doi: 10.18323/2782-4039-2025-3-73-4

Microstructure, properties and strengthening mechanisms of low-carbon steel subjected to equal-channel angular pressing

Andrey V. Malinin*[1,3], PhD (Engineering),
Deputy General Director for Research
Vil D. Sitdikov[1,4], Doctor of Sciences (Physics and Mathematics),
senior expert
Yuri A. Lebedev[2], PhD (Physics and Mathematics),
senior researcher

[1]*LLC RN-BashNIPIneft, Ufa (Russia)*
[2]*Institute of Physics of Molecules and Crystals of Ufa Federal Research Center of RAS, Ufa (Russia)*

***E-mail:** MalininAV@bnipi.rosneft.ru

[3]ORCID: https://orcid.org/0000-0003-1185-5648
[4]ORCID: https://orcid.org/0000-0002-9948-1099

Received 22.07.2025 *Revised 29.07.2025* *Accepted 20.08.2025*

Abstract: In the work, an ultrafine-grained (UFG) state was formed in a low-carbon steel by equal-channel angular pressing (ECAP) (8 passes, 200 °C), demonstrating high mechanical properties (yield strength is 1021 MPa, tensile strength is 1072 MPa, ductility is 10.7 %) along with satisfactory corrosion resistance (0.345 mm/year). To explain the reasons for improvement of strength properties and changes in corrosion properties, UFG steel microstructure was analysed using electron microscopy and X-ray scattering methods. Specifically, electron microscopy methods revealed structural refinement of ECAP-processed steel, resulting in the formation of equiaxed grains averaged ~240 nm in size. Modified Williamson–Hall and Warren–Averbach X-ray procedures were applied to find the patterns of changes in coherent scattering domains size, density ρ and fraction f_s of screw-type dislocations, effective outer cut-off radius R_e of dislocations and some other parameters of low-carbon steel depending on a number of ECAP passes (degree of deformation). X-ray diffraction analysis and small-angle X-ray scattering methods were used to determine evolution trends of mass fraction, size and morphology of various precipitates depending on the number of ECAP passes. Based on the obtained data, a model of microstructure transformation during UFG state formation in steel was proposed. Furthermore, strengthening mechanisms of both coarse-grained and UFG steels were discussed. It was found that in initial state, steel strength was primarily ensured by grain-boundary strengthening and precipitation of small $Me_{23}C_6$ and Me_3C_2 precipitates. It was shown that during UFG structure formation, steel strength increases due to grain-boundary strengthening and dislocation density increase. The contribution of precipitates in the UFG state to the strengthening decreases and this is due to their growth during ECAP processing. It was found that an increase in corrosion rate of UFG steel results from a decrease in ferrite grain size, an increase in grain-boundary dislocations density and a cellular structure formation.

Keywords: low-carbon steel; ferrite; equal-channel angular pressing; ultrafine-grained structure; microstructure; strengthening mechanisms; X-ray diffraction analysis; corrosion rate; small-angle X-ray scattering.

Acknowledgments: The authors express their gratitude to PJSC Rosneft Oil Company and LLC RN-BashNIPIneft for the opportunity to conduct the research. The authors also thank A.I. Voloshin, Doctor of Sciences (Chemistry), Yu.B. Lind, PhD (Physics and Mathematics), and N.R. Yarkeeva, PhD (Engineering) (LLC RN-BashNIPIneft) for discussing the results obtained and valuable comments during the preparation of the paper.

For citation: Malinin A.V., Sitdikov V.D., Lebedev Yu.A. Microstructure, properties and strengthening mechanisms of low-carbon steel subjected to equal-channel angular pressing. *Frontier Materials & Technologies*, 2025, no. 3, pp. 51–65. DOI: 10.18323/2782-4039-2025-3-73-4.

INTRODUCTION

Currently, low-carbon steels are widely used in the automotive, construction, aerospace and oil and gas industries due to their high industrial application potential. Nevertheless, further enhancement of the set of physical, mechanical and performance properties of low-carbon steels through the optimisation of alloying elements and/or the implementation of various thermomechanical processing modes remains a significant fundamental and applied challenge in materials science. To date, among the various methods for improving the physical and mechanical properties of metallic materials and alloys, the methods of severe plastic deformation (SPD) are among the most popular [1–4]. As a result of SPD processing, an ultrafine-grained (UFG) structure is formed in the initial coarse-grained (CG) metallic materials due to the refinement of the initial grains [1–4]. Moreover, UFG structures produced by SPD methods in metals and alloys are characterised by an increased density of introduced defects, products of various phase transformations, the formation of equiaxed grains of nanometric size and highly non-equilibrium grain boundaries [5; 6]. Furthermore, in the case of SPD effects on alloys, dynamic strain ageing may occur in them, resulting in the precipitation of particles of different morphology, sizes and chemical compositions in the main phase [7; 8]. All these microstructural changes in metals and alloys processed by such techniques lead to the formation of high-strength states due to the activation of various strengthening mechanisms [9; 10]. In this regard, the creation of high-strength steels through targeted control of their structure and phase composition represents a pressing issue in modern materials science.

The main SPD methods include equal-channel angular pressing (ECAP) and high-pressure torsion (HPT) [1; 2]. Previously, these methods have been successfully applied to obtain high-strength states in a number of low-carbon steels [11–13]. In particular, the authors of [11] applied the ECAP method to AISI 1010 steel with three passes at a temperature range of 150–300 °C. By varying the ECAP temperature, they obtained a high-strength state of the steel at 200 °C, characterised by high yield strength σ_{YS} of 778 MPa and ultimate tensile strength σ_{UTS} of 819 MPa, significantly exceeding those of the CG steel (σ_{YS}=252 MPa, σ_{UTS}=307 MPa) [11]. At the same time, ductility decreased by more than half. The improvement in strength characteristics was attributed by the authors to the formation of a ferritic UFG structure in the steel [11]. In [12], the authors managed to increase the number of ECAP passes (degree of deformation) in ferritic steel up to six by raising the temperature to 300 °C. It was shown [12] that increasing the ECAP deformation degree further raised the yield strength to 851 MPa and the ultimate tensile strength to 857 MPa. However, the ductility value did not exceed 9 %. Based on microstructural analysis, it was concluded that the formation of a banded structure consisting of submicrocrystalline grains with high dislocation density enhances the mechanical properties of ferritic steel [12]. Furthermore, hot rolling of low-carbon steel prior to ECAP processing allowed increasing the number of passes up to ten [13]. Thanks to such combined processing, the authors succeeded in forming a banded structure composed of elongated grains with a width of 200–300 nm, thereby raising the ultimate tensile strength to record-high values (over 1200 MPa) [13].

When determining the reasons for the improvement of strength characteristics in ECAP-processed steels, the authors [11–13] relied solely on electron microscopy data. Meanwhile, X-ray scattering methods are a powerful tool for providing an integrated characterisation of the steel microstructure through other structural parameters [14–16]. Recently modified Williamson–Hall and modified Warren–Averbach techniques have been successfully applied to the structural characterisation of steels [17; 18]. In particular, the reasons for the destruction of the near-surface layer of martensitic steel were identified, which included the reduction in dislocation density, a change in the dislocation type and an increase in the coherent scattering domain (CSD) size [17]. In [18], X-ray scattering was used to study the changes in microstructural parameters during the tensile deformation of Fe–26Mn–1Al–0.14C steel. It was found that tensile deformation leads to an increase in dislocation density, suppression of the screw dislocations shares, the emergence of a strong dislocation dipole field indicative of cell structure formation and the activation of dynamic recovery (growth of the effective outer cut-off radius of dislocations) [18].

The above examples demonstrate that the combined use of X-ray scattering and electron microscopy methods enables a more detailed characterisation of steel structures during thermomechanical processing. Accordingly, in the present study, these methods were jointly applied to determine the reasons for the enhancement of strength properties and changes in corrosion behaviour in a medium-carbon steel upon the formation of a UFG state.

Objective of the study is to form a high-strength state in medium-carbon steel using the ECAP method, to analyse strengthening mechanisms and to identify possible reasons for changes in corrosion properties based on microstructural data obtained by X-ray scattering and electron microscopy methods.

METHODS

Methodology for the UFG structure formation

A widely used low-carbon steel was selected for the formation of UFG structure by ECAP method. The chemical composition of the steel measured by optical emission spectrometry is presented in Table 1. Before ECAP processing, the cylindrical steel specimens (9 mm in diameter and 30 mm in length) were annealed at a temperature of 200 °C for 1 h. ECAP was performed using tooling with a channel intersection angle of 120°. The ECAP processing temperature was maintained at 200 °C, the deformation route used was route B_C and the number of passes was 4, 6, and 8.

Table 1. *Chemical composition of the studied steel (wt. %)*
Таблица 1. *Элементный состав исследуемой низкоуглеродистой стали (мас. %)*

C	Si	Mn	Cr	Ni	Cu	P	S	Fe
0.108	0.195	0.397	0.135	0.216	0.087	0.003	0.012	balance

Methodology for carrying out mechanical and corrosion tests

Tensile mechanical tests were carried out using a universal testing machine Instron 8801. The following mechanical properties were determined: yield strength σ_{YS}, ultimate tensile strength σ_{UTS} and elongation δ. In order to exclude the influence of the heterogeneity of the formed structure and the effects of poor processing of the peripheral areas, tests were carried out on small samples cut from the central area of the rod relative to its longitudinal axis [1; 3]. The dimensions of the flat samples: length 4 mm, sides of the working part 1×1 mm^2. The strain rate during tensile testing was $1\cdot10^{-3}$ s^{-1}. The steel hardness after various numbers of ECAP passes was measured using the Vickers method on a universal hardness tester Shimadzu HMV-G with an indenter load of 100 g and a dwell time of 10 s.

Corrosion rate V_c was determined by mass loss after exposure to a corrosive environment. For corrosion testing, disks 9 mm in diameter and 2 mm thick were cut from the as-received and ECAP-processed specimens. Samples were kept in a test solution prepared from 5.0 wt. % sodium chloride, 0.5 wt. % acetic acid and distilled water for 100 h.

Methodology for studying microstructure using electron microscopy

The microstructure of the as-received and ECAP-processed specimens was analysed using a scanning electron microscope (SEM) Thermo Scientific Q250 (USA). Microstructure analysis was performed on cross-sectional metallographic specimens cut from ECAP-processed samples. Specimens were prepared for SEM by grinding, followed by polishing with diamond paste and etching in a nital solution. The steel microstructure was also examined by transmission electron microscopy (TEM) to obtain information on the size of structural elements, with an accelerating voltage of 200 kV. Thin foils for TEM studies were prepared by twin-jet electropolishing using an electrolyte based on *n*-butyl alcohol.

Methodology for carrying out X-ray structural analysis

X-ray diffraction analysis (XRD) was performed on steel samples using a Tongda TD-3000 diffractometer (China) operating in Bragg–Brentano geometry. X-ray patterns were recorded within a 2θ scattering angle range from 25° to 140° in continuous scanning mode at a scanning speed of 0.5 °/min. Cu anode tube was used to generate radiation (λ=0.154060 nm) at an operating voltage of 40 kV and a current of 35 mA. Diffracted beams were detected using a Mythen 2D multichannel detector (Switzerland). Parasitic β and W_L lines from copper radiation were suppressed using a 30 μm thick nickel foil. The use of a high-precision multichannel detector and nickel foil in the registration of diffracted copper radiation reduced fluorescence levels on the X-ray patterns, enabling the measurement of clear (*hkl*) reflections both from ferritic steel and from secondary phases.

The calculation of fine structure parameters (CSD average size D, dislocation density ρ, fraction of screw-type dislocations, effective outer cut-off radius R_e and dislocation type) was carried out using the modified Williamson–Hall (mW-H) and Warren–Averbach (mW-A) techniques [19]. In the mW-H method, CSD size $D_{W\text{-}H}$ was determined based on the full width at half maximum (FWHM) broadening according to the dependence of $\Delta K = FWHM\,\frac{\cos\theta}{\lambda}$ on $K=\frac{2\sin\theta}{\lambda}$:

$$\Delta K = \frac{0{,}9}{D} + \left(\frac{\pi M^2 b^2}{2}\right)^{\frac{1}{2}} \rho^{\frac{1}{2}} \left(K\overline{C}^{\frac{1}{2}}\right) + O\left(K^2\overline{C}\right), \tag{1}$$

where K is the scattering vector;
M is the Wilkens parameter depending on the effective outer cut-off radius R_e of dislocations;
$\overline{C}$ is the average dislocation contrast factor;
b is the value of the Burgers vector (0.204 nm).

By squaring equation (1) and considering that $(O(K^2\overline{C}))^2\approx0$, the following expression for calculating $D_{W\text{-}H}$ was obtained:

$$\frac{\Delta K^2-\alpha}{K^2} = \frac{\pi M^2 b^2}{2}\,\rho\overline{C}_{h00}\left(1-qH\right), \tag{2}$$

where $\overline{C}_{h00}$ is the average dislocation contrast factor in the $\{h00\}$ plane;
q is a constant related to the type of dislocations and the elastic constants of steel;
H for an arbitrary $\{hkl\}$ plane was determined using the expression

$$H = \frac{h^2k^2+h^2l^2+k^2l^2}{h^2+k^2+l^2};$$

$$\alpha = \left(\frac{0{,}9}{D}\right)^2.$$

The dislocation density ρ used in equation (2) was found from the real $A(L)$ and size $A^s(L)$ parts of the Fourier coefficients (where L is Fourier length) using the mW-A method:

$$\begin{aligned}\ln A(L) &= \ln A^s(L) - \frac{\pi b^2\rho}{2}L^2\ln\left(\frac{R_e}{L}\right)\left(K^2\overline{C}\right) = \\ &= \ln A^s(L) - YK^2\overline{C}\end{aligned}, \tag{3}$$

where $Y=\frac{\pi b^2\rho}{2}L^2\ln\left(\frac{R_e}{L}\right)$.

By transforming equation (3), a relation for determining ρ was obtained:

$$\frac{Y}{L^2} = \frac{\pi b^2\rho}{2}L^2\ln\left(\frac{R_e}{L}\right) - \rho\frac{\pi b^2}{2}\ln(L). \tag{4}$$

Equations (3) and (4) are similar to the expression $y=m+(-k)x$. Accordingly, $A^S(L)$ values were determined by approximating the dependence of ln$A(L)$ on $K^2\overline{C}$ to the point of intersection with the OY-axis (i. e., the $\ln A(L)$ axis). From this dependence (4), values of Y were also determined via the tangent of the curve slope. Dislocation density ρ values used in the right part of equation (4) were found from the graph of Y/L^2 versus $\ln(L)$ based on the tangent of the curve slope. R_e value for each state was determined by approximating the graph of relation (4) to the point of intersection with the OY axis. Instrumental broadening of steel (*hkl*) reflections was taken into account by recording and analysing the X-ray pattern of LaB_6 powder.

Small-angle X-ray scattering technique

To obtain information about the morphology and size of precipitates, thin foils were prepared from thin sections (5 mm long, 10 mm wide, ~20 µm thick). Small-angle X-ray scattering (SAXS) curves were recorded in the scattering vector q range from 0.01 to 1.4 nm^{-1} using Tongda TD-3000 diffractometer (China) equipped with a single-channel detector. The diameter of the analysed foil surface was ~3.5 mm. When analysing the steel precipitates, the resulting scattering intensity $I(q)$ was expressed as:

$$I(q) = I(q)_1 + I(q)_2 + \ldots + I(q)_n = \sum_{i=1}^{n} \left|F(q)_i^2\right|\left|S(q)_i^2\right|,$$

where $I(q)_i$ is the scattering intensity from precipitates with the i-th shape;

$F(q)_i$ is the form factor defining the morphology of the i-th precipitates;

$S(q)_i$ is the structure factor determining the spatial distribution of the i-th precipitates.

The morphology of the precipitates was defined according to the expressions given in [20].

RESULTS

Tensile and corrosion resistance tests

The results of mechanical tests and corrosion rate data for the studied steel states are presented in Table 2. It can be seen that ECAP processing of the initial steel leads to an increase in its hardness and strength characteristics (Table 2). In particular, after 4 ECAP passes, the steel hardness increases by 1.4 times, yield strength σ_{YS} increases by 2.9 times and ultimate tensile strength σ_{UTS} increases by 2.3 times compared to the initial CG state. At the same time, an inverse effect is observed: the steel ductility decreases by approximately 2.7 times. This state is also characterised by an increase in corrosion rate by 0.03 mm/year. An increase in the number of ECAP passes to 6 results in a further growth of microhardness, tensile strength, yield strength, and corrosion rate (Table 2). The steel ductility in this state slightly improves. After 8 ECAP passes, the steel exhibits very high strength properties, with ductility reaching ~11 % (Table 2). The corrosion rate after 8 ECAP passes increases by 0.046 mm/year.

Microstructure studies using electron microscopy

SEM images of the microstructure of the initial and ECAP-processed steels are shown in Fig. 1. In the initial state, the steel microstructure is characterised by the presence of ferrite grains (Fig. 1 a). In some ferrite grains, needle-like cementite particles are also visible. The average ferrite grain size, based on the analysis of no fewer than ten images, was ~4 µm. As a result of ECAP processing (4 passes), a banded structure is formed in the steel (Fig. 1 b). The bands contain heavily refined grains (average size ~270 nm according to TEM data), in which a high density of defects in the form of dislocation tangles can also be observed (Fig. 1 b, inset). After 6 ECAP passes, the banded structure becomes less pronounced (Fig. 1 c). The average ferrite grain size in this state, based on TEM investigations, was ~250 nm (Fig. 1 c, inset). After 8 ECAP passes, the steel forms an equiaxed structure with an average grain size of ~240 nm (Fig. 1 d). Additionally, a cellular structure is observed in some grains (Fig. 1 d, inset).

Microstructure studies using X-ray diffraction analysis

Experimental X-ray patterns of the steel in various structural states are presented in Fig. 2. It is evident that the X-ray patterns for the initial and ECAP-processed states

***Table 2.** Mechanical properties and corrosion rate of low-carbon steel in coarse-grained and ultrafine-grained states*

***Таблица 2.** Механические свойства и скорость коррозии низкоуглеродистой стали в крупнокристаллическом и ультрамелкозернистом состояниях*

State	HV, GPa	σ_{YS}, MPa	σ_{UTS}, MPa	δ, %	V_c, mm/year
CG	1.89±0.08	343±9	454±8	26.1±1.3	0.299±0.006
ECAP, 4 passes	2.66±0.06	995±10	1033±6	9.7±0.5	0.329±0.008
ECAP, 6 passes	2.77±0.04	1012±8	1061±9	9.9±0.4	0.336±0.006
ECAP, 8 passes	2.85±0.05	1021±9	1072±12	10.7±0.4	0.345±0.005

Note. HV is Vickers hardness; σ_{YS} is yield strength; σ_{UTS} is ultimate strength; δ is plasticity; V_c is corrosion rate.

Примечание. HV – твердость по Виккерсу; σ_{YS} – предел текучести; σ_{UTS} – предел прочности; δ – пластичность; $V_к$ – скорость коррозии.

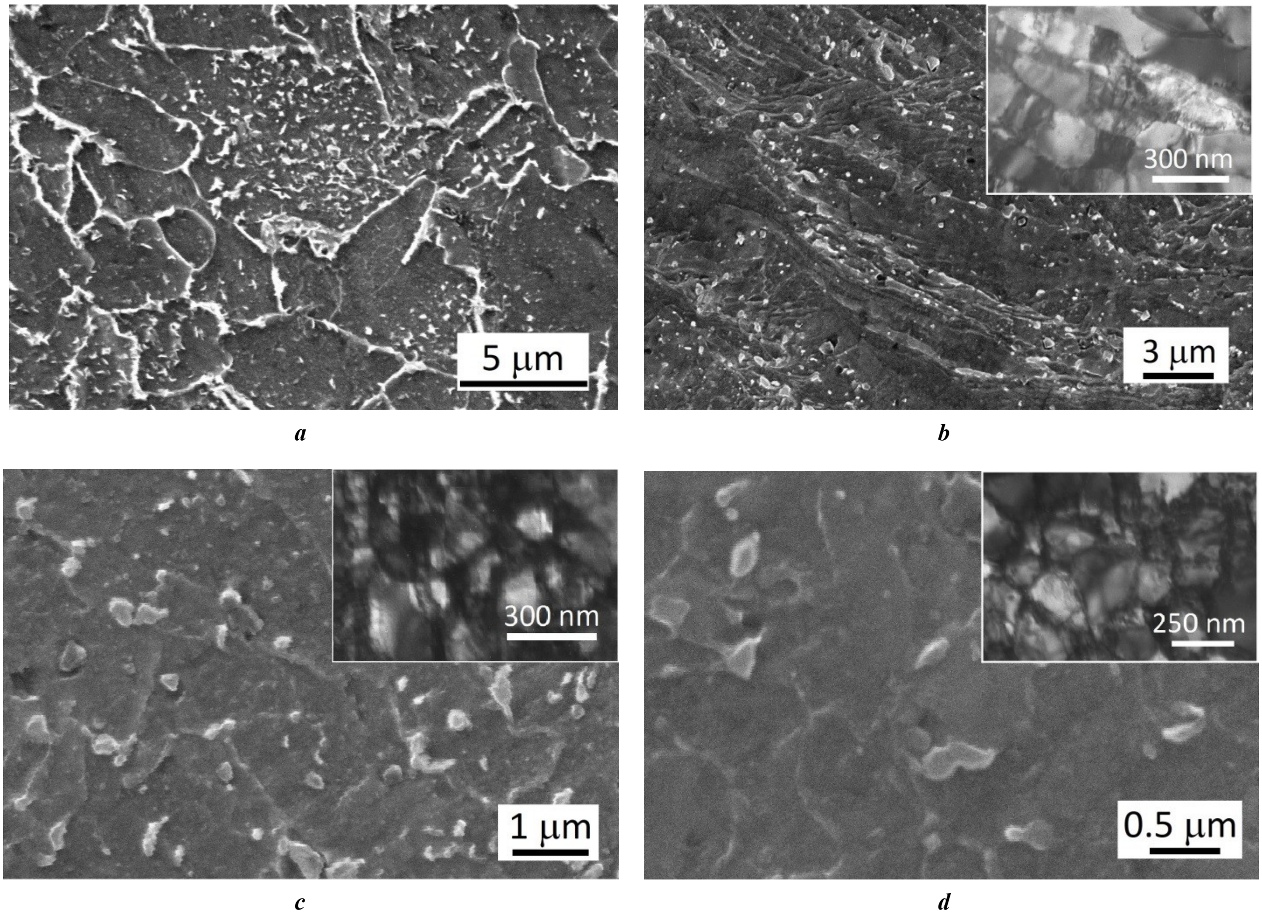

Fig. 1. *SEM images of the microstructure of the steel under study:*
a *– in the coarse-grained state;* ***b*** *– after 4 ECAP passes;* ***c*** *– after 6 ECAP passes;*
d *– after 8 ECAP passes. The insets contain TEM images*

Рис. 1. *РЭМ-изображения микроструктуры исследуемой стали:*
a *– крупнокристаллическое состояние;* ***b*** *– после 4 проходов РКУП;* ***c*** *– после 6 проходов РКУП;*
d *– после 8 проходов РКУП. Во вставках изображения, полученные ПЭМ*

are characterised by the presence of ferrite (α-Fe) reflections and cementite (Fe_3C) particles (Fig. 2 a). At the same time, new reflections appear on the X-ray pattern of a sample after ECAP (4 passes) (Fig. 2 a).

Phase identification revealed that these new reflections belong to $Me_{23}C_6$- and Me_3C_2-type precipitates. An increase in the number of ECAP passes leads to a growth in the intensity of $Me_{23}C_6$ and Me_3C_2 reflections on the X-ray patterns (Fig. 2 a). To evaluate the mass fraction of the identified phases, Rietveld refinement was performed on the X-ray patterns. An example of such refinement is shown in Fig. 2 b. Minor fluctuations in the difference curve (grey) between the measured (black) and the simulated (red) X-ray patterns indicate a good correlation between them. The results of the X-ray analysis regarding the content of identified phases are presented in Table 3.

The initial steel is characterised by a relatively high content of cementite Fe_3C particles and a low mass fraction of $Me_{23}C_6$ precipitates. During the formation of the UFG structure in steel, the mass fractions of $Me_{23}C_6$ and Me_3C_2 precipitates increase, while the cementite particle content remains practically unchanged (Table 3).

Precise analysis of the X-ray patterns revealed that, in addition to the appearance and growth of $Me_{23}C_6$ and Me_3C_2 reflections, an increase in broadening of the ferrite (*hkl*) reflections and a shift toward higher angles occur as a result of ECAP processing. These changes are clearly illustrated in Fig. 3 using the (110) and (210) ferrite reflections as examples.

Additionally, the insets in Fig. 3 b show the (200) and (320) reflections of lanthanum hexaboride used to take into account the contribution of instrumental broadening of the (110) and (211) ferrite peaks. As is known [21], an increase in peak broadening indicates a rise in defect density in the fine structure and a decrease in the CSD size *D*, while a peak shift toward large angles leads to a decrease in the lattice parameter. In this regard, these microstructural changes were further analysed by means of XRD analysis. To estimate the CSD size and dislocation type, the mW-H technique (Equation (2)) was used, and for the evaluation of the effective outer cut-off radius of dislocations and Wilkens parameter, the mW-A technique was used (Equation (4)).

In order to find the $\overline{C}_{h00}$ value in Equation (2), contrast factors $\overline{C}^{e}_{hkl}$ for edge and screw $\overline{C}^{s}_{hkl}$ dislocations were calculated according to [22]. For the investigated steel grade, the elastic constants C_{11}, C_{12} and C_{44} are 245, 139 and 122 GPa, respectively [23]. The calculated values of $\overline{C}^{e}_{hkl}$ and $\overline{C}^{s}_{hkl}$ are presented in Table 4. Based on these

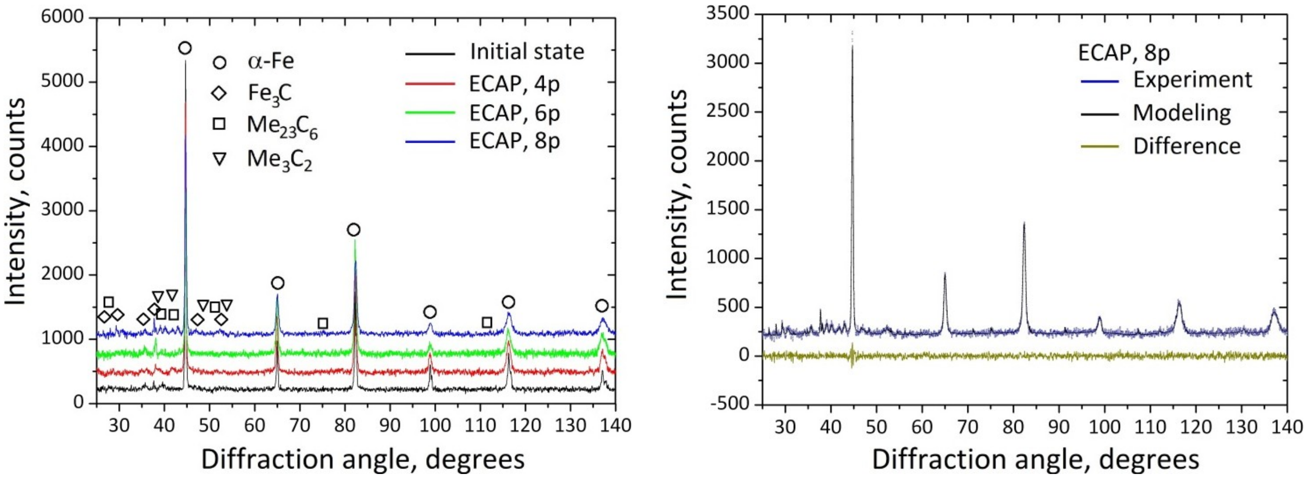

a ***b***

Fig. 2. *Experimental diffraction patterns of steel in different structural states:*
a *– general view;* ***b*** *– processed diffraction pattern of steel after 8 ECAP passes*
Рис. 2. *Экспериментальные дифрактограммы стали в различных структурных состояниях:*
a *– общий вид;* ***b*** *– обработанная дифрактограмма стали после 8 проходов РКУП*

Table 3. *Identified phases and their mass fraction in the original and ultrafine-grained low-carbon steel*
Таблица 3. *Обнаруженные фазы и их массовая доля в исходной и ультрамелкозернистой низкоуглеродистой стали*

State	**Mass fraction of phases, %**			
	α-Fe	**Fe_3C**	**$Me_{23}C_6$**	**Me_3C_2**
CG	99.24±0.54	0.76±0.07	0.13±0.07	–
ECAP, 4 passes	98.72±0.61	0.82±0.06	0.34±0.05	0.12±0.05
ECAP, 6 passes	98.45±0.49	0.85±0.04	0.54±0.06	0.16±0.05
ECAP, 8 passes	98.36±0.55	0.81±0.04	0.62±0.05	0.21±0.06

data, theoretical values of q^e_{th} and q^s_{th} were estimated, which turned out to be 1.29 and 2.44, respectively. To determine the value of q, the parameter α in Equation (2) was optimised to obtain a linear relationship, as shown in Fig. 4 a. By approximating the dependencies shown in Fig. 4 a to the intersection with the OX axis, the values of $1/q$ were obtained for each state (q=2.25, 1.94, 1.81, and 1.66 for the initial CG state, and after 4, 6, and 8 ECAP passes, respectively). The fractions f_e of edge and f_s of screw dislocations were then determined according to the expression

$$q = (1 - f_s)q^e_{th} + f_s q^s_{th}.$$

The obtained values made it possible to find $\bar{C}_{h00}$ using the formula

$$\bar{C}_{h00} = (1 - f_s)\bar{C}^e_{h00} + f_s \bar{C}^s_{h00}.$$

The averaged $\bar{C}_{hkl}$ values were calculated according to formula (Table 4)

$$\bar{C}_{hkl} = \bar{C}_{h00}(1 - qH).$$

Based on the obtained data, the dependence $\Delta K(K\bar{C}^{1/2})$ was plotted as shown in Fig. 4 b. Extrapolation of $\Delta K(K\bar{C}^{1/2})$ dependence to its intersection with the OY axis allowed estimating the $D_{W\text{-}H}$ CSD size according to the mW-H technique. Resulting $D_{W\text{-}H}$ CSD size values and the fractions of screw dislocations for the studied states are summarised in Table 5.

To assess the dislocation density in the mW-A technique, Fourier coefficients were first determined by analysing each reflection on the X-ray pattern of the initial and ECAP-processed steel.

Examples of the obtained Fourier coefficients Ln$A(L)$ as functions of $K^2\bar{C}$ (equation 3) for the initial and UFG steel (8 ECAP passes) are shown in Fig. 5 a, b. Subsequently, based on the ln$A(L)$ vs $K^2\bar{C}$ dependencies and by approximating the lines to their intersection with the OY axis (see insets in the figures), the dimensional values $A^s(L)$ of the Fourier coefficients were determined. These coefficients for the studied steel states are presented in Fig. 5 c as $A^s(L)$ dependencies.

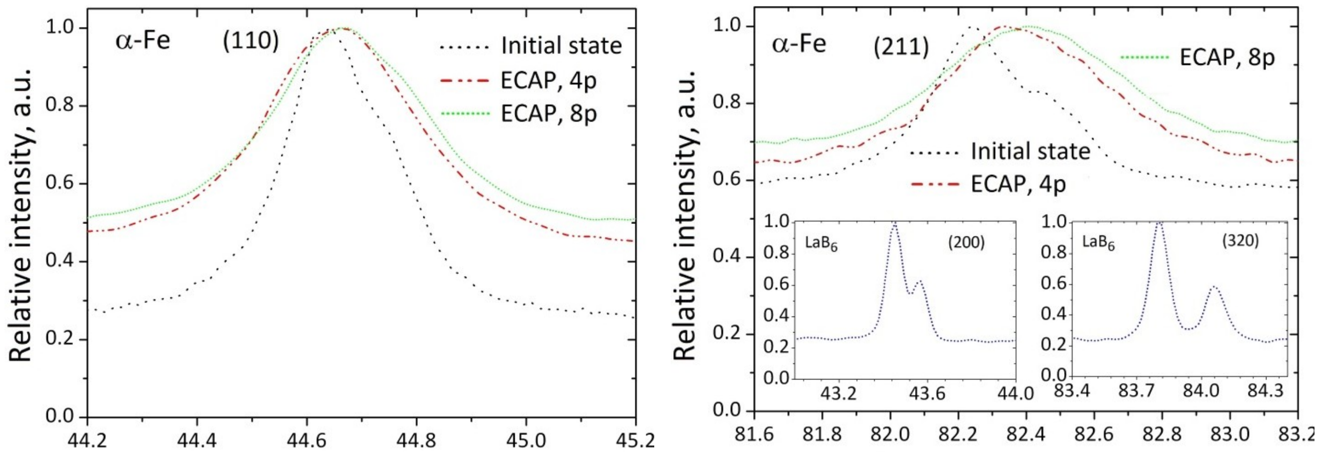

a ***b***

Fig. 3. *Normalised reflections of steel demonstrating the change in their width and angular position on the diffraction pattern:* ***a*** *– reflection (110);* ***b*** *– (211).*
The insets show some reflections of LaB_6, which were used to take into account the instrumental broadening of the peaks

Рис. 3. *Нормализованные рефлексы стали, демонстрирующие изменение их ширины и угловой позиции на дифрактограмме:* ***a*** *– отражение (110);* ***b*** *– (211).*
Во вставках приведены некоторые рефлексы LaB_6, по которым учитывали инструментальные уширения пиков

Table 4. *Calculated values of* $\overline{C}^{e}_{hkl}$, $\overline{C}^{s}_{hkl}$ *and* $\overline{C}_{hkl}$ *for coarse-grained and ECAP steel*

Таблица 4. *Рассчитанные для крупнокристаллической и подвергнутой РКУП стали значения* $\overline{C}^{e}_{hkl}$, $\overline{C}^{s}_{hkl}$ *и* $\overline{C}_{hkl}$

Plane (*hkl*)	$\overline{C}^{e}_{hkl}$	$\overline{C}^{s}_{hkl}$	$\overline{C}_{hkl}$			
			CG	**ECAP, 4 passes**	**ECAP, 6 passes**	**ECAP, 8 passes**
(110)	0.172182	0.118142	0.05568	0.06202	0.06469	0.06776
(200)	0.252323	0.37929928	0.35786	0.32378	0.30949	0.29300
(211)	0.172182	0.118138	0.05568	0.33083	0.06468	0.06776
(220)	0.172182	0.118142	0.05568	0.33084	0.05797	0.06776
(310)	0.223471	0.204317	0.16551	0.16960	0.17132	0.17330
(222)	0.145468	0.0732345	0.02200	0.02699	0.02908	0.03150

By drawing tangents to the obtained curves in the domain of small L values, $D_{W\text{-}A}$ CSD size for the different structural states of steel was determined. Further, using the obtained Fourier coefficients $A^s(L)$, the dependence Y/L^2 vs $\ln L$ (Fig. 5 d) was plotted. From this dependence, in accordance with equation 4, the dislocation density was calculated. By approximating the curves (Fig. 5 d) to their intersection with the OY axis (at $\ln L$=0), the effective outer cut-off radius of dislocations R_e was determined. The resulting information on the fine structure parameters is presented in Table 5.

Analysis of Table 5 shows that an increase in the number of ECAP passes leads to a decrease in the lattice parameter, a decrease in the CSD parameter, an increase in the dislocation density, and a decrease in the proportion of screw-type dislocations. At the same time, a decrease in the R_e and M values indicates an increase in dislocation dipole fields, and the nature of the mutual arrangement of dislocations becomes ordered.

Microstructure studies using small-angle X-ray scattering

To obtain dimensional characteristics of the precipitates (Fe_3C, $Me_{23}C_6$, Me_3C_2) identified during phase analysis, measurement and analysis of SAXS curves were carried out for the investigated states. Experimental SAXS curves for CG and UFG states of the steel, as well as an example of processed scattering curve after 8 ECAP passes, are shown in Fig. 6. Unlike the scattering curve for CG steel, the UFG SAXS curves are characterised by pronounced inflection

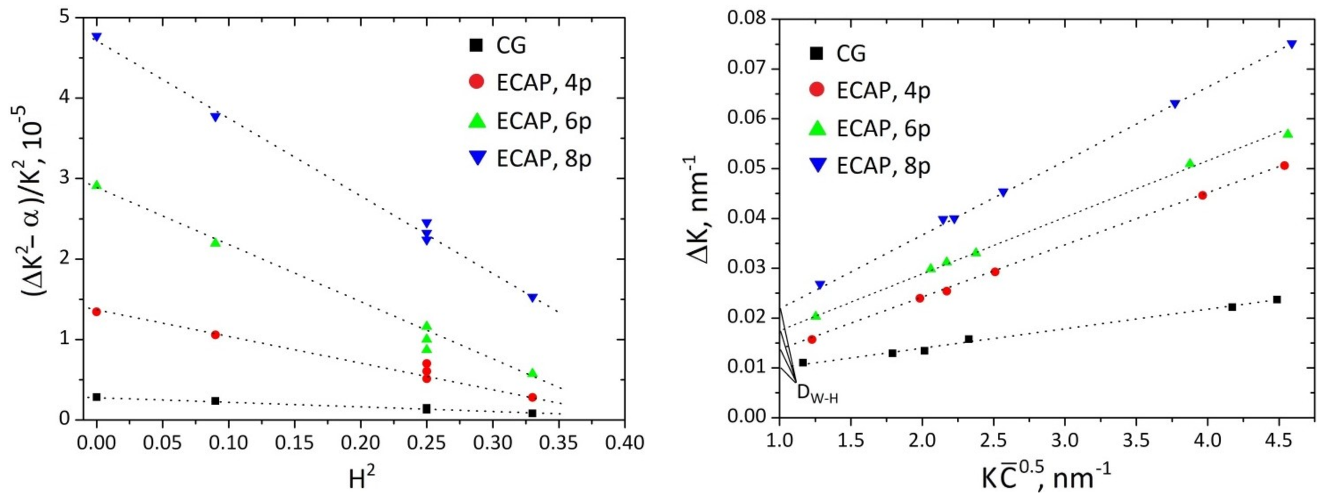

a *b*

Fig. 4. *Experimental dependencies for various structural states of steel in the modified Williamson–Hall method:* ***a*** *–* $\frac{\Delta K^2-\alpha}{K^2}$ *vs* H^2*;* ***b*** *–* ΔK *vs* $K\bar{C}^{1/2}$

Рис. 4. *Экспериментальные зависимости для различных структурных состояний стали по модифицированной методике Вильямсона – Холла:* ***a*** *–* $\frac{\Delta K^2-\alpha}{K^2}$ *от* H^2*;* ***b*** *–* ΔK *от* $K\bar{C}^{1/2}$

Table 5. *Fine structure parameters of steel in the initial state and after ECAP*

Таблица 5. *Параметры тонкой структуры стали в исходном состоянии и в состояниях после РКУП*

State	a, nm	D_{W-H}, nm	D_{W-A}, nm	ρ, 10^{15} m^{-2}	f_s, %	R_e, nm	M
CG	0.286808±0.000012	229±20	356±24	0.11±0.03	83±4	184±15	1.94±0.11
ECAP, 4 passes	0.286769±0.000009	88±5	53±3	1.93±0.02	56±3	14±2	0.63±0.05
ECAP, 6 passes	0.286732±0.000011	79±4	48±2	2.68±0.02	45±3	8±1	0.41±0.04
ECAP, 8 passes	0.286692±0.000013	61±4	43±2	3.32±0.03	32±2	6±1	0.33±0.03

Note. a is the lattice parameter;
D_{W-H} *is the CSD size found in modified Williamson–Hall (mW-H);*
D_{W-A} *is the CSD size found in modified Warren–Averbach (mW-A) technique; ρ is the dislocation density;*
f_s *is the fraction of screw-type dislocations;* R_e *is the effective outer radius of the dislocation cross-section;*
M is the Wilkens parameter.

Примечание. a – параметр решетки;
D_{W-H} *– размер ОКР, найденный по модифицированной методике Вильямсона – Холла;*
D_{W-A} *– размер ОКР, найденный по модифицированной методике Уоррена – Авербаха;*
ρ – плотность дислокаций; f_s *– доля дислокаций винтового типа;* R_e *– эффективный внешний радиус сечения дислокаций;*
M – параметр Вилкенса.

points concentrated in the Guinier region (range 0.05 to 0.5 nm^{-1}) (Fig. 6 a). Moreover, in this region, the UFG steel scattering curves show a sharp decrease in intensity depending on scattering vector (Fig. 6 a).

It is known that the particle size is determined by the position of the Guinier region on the SAXS curve and particle morphology is determined through the dependence $I \sim q^{-\alpha}$, where α parameter equals 1, 2, 3, or 4 (particle shapes: α=1 (cylinder), 2 (disk), 3 and 4 (sphere)) [24]. Analysis showed that, in the CG state, the Guinier region is characterised by a dependence $I \sim 1/q$, indicating that the initial steel mainly contains particles of cylindrical shape. In the case of ECAP steel, it was found that the area from 0.05 to 0.5 nm^{-1} does not conform to the known dependences described above. Therefore, when analysing the SAXS curves of ECAP-processed steel, three types of particles differing in morphology (Table 3) were simultaneously fitted into the model. The result of such processing, e. g. for the 8 ECAP state, is shown in Fig. 6 b. It is evident that

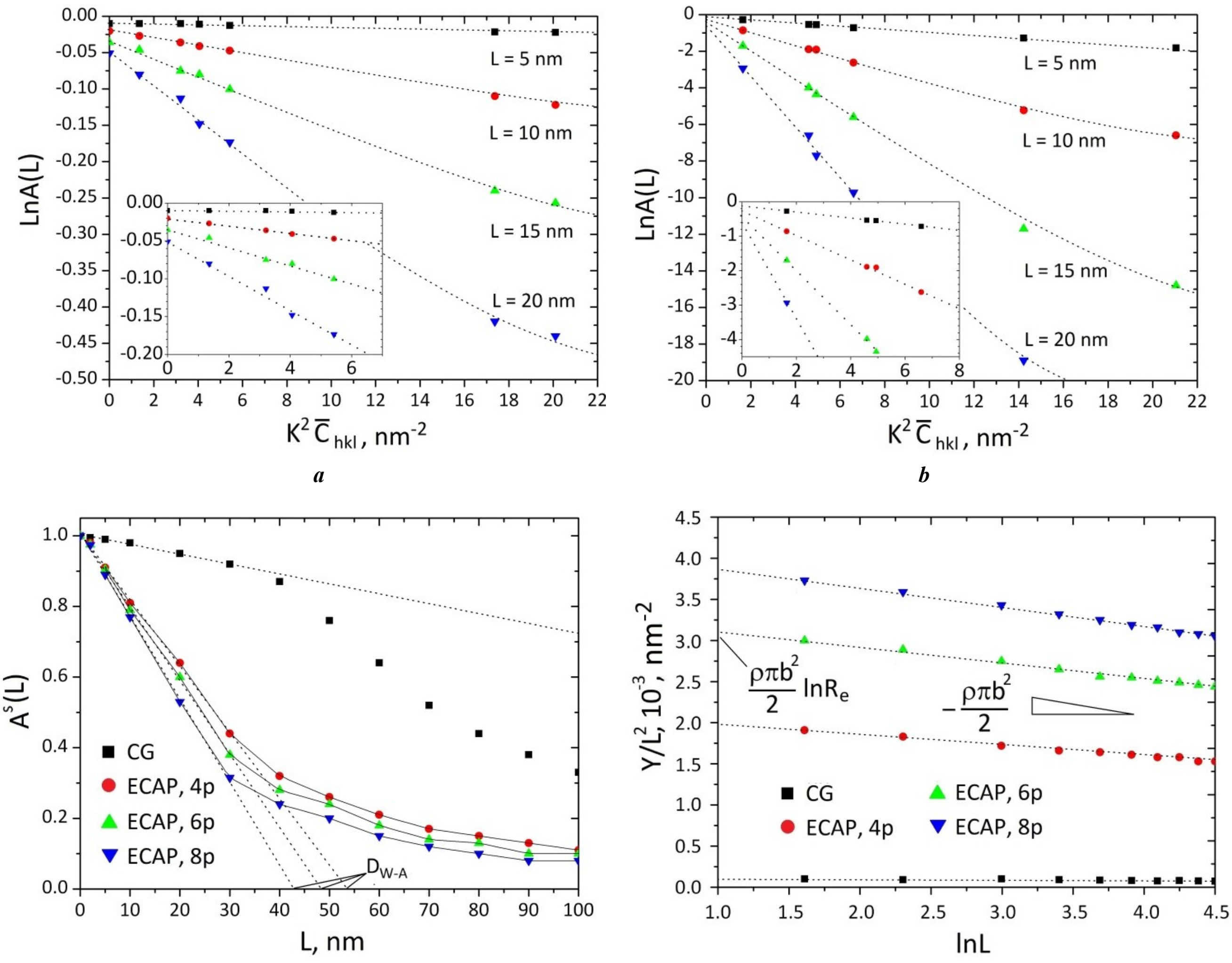

a

b

c

d

Fig. 5. *Experimental dependencies for various structural states of steel in the modified Warren–Averbach method:*
a *– lnA(L) on $K^2\overline{C}$ for the initial steel;* ***b*** *– lnA(L) on $K^2\overline{C}$ for UFG steel (8 ECAP passes);* ***c*** *– $A^s(L)$ patterns;*
d *– Y/L^2(lnL) dependence for different structural states of steel.*
The insets show enlarged areas where the As(L) coefficients were found

Рис. 5. *Экспериментальные зависимости для различных структурных состояний стали*
по модифицированной методике Уоррена – Авербаха:
a *– lnA(L) от $K^2\overline{C}$ для исходной стали;* ***b*** *– lnA(L) от $K^2\overline{C}$ для ультрамелкозернистой стали (8 проходов РКУП);*
c *– закономерности $A^s(L)$;* ***d*** *– зависимость Y/L^2(lnL) для различных структурных состояний стали.*
Во вставках показаны увеличенные области, по которым находили коэффициенты $A^s(L)$

this approach allows modelling satisfactory the experimental SAXS curves of the UFG steel leading to the determination of particle size and shape (Table 6).

Moreover, this analysis makes it possible to determine the contributions of individual particle types to the resulting SAXS intensity. Specifically, in Fig. 5 b, one can see that the SAXS intensity from cylindrical Fe_3C particles is higher than that from spherical Me_3C_2-type particles. This fact indicates a higher fraction of cementite particles compared to Me_3C_2-type particles, which is consistent with the data in Table 3.

The SAXS analysis revealed that the particle sizes in CG steel are significantly smaller than those in UFG steel (Table 6). Furthermore, an increase in the number of ECAP passes is accompanied by a growth in the sizes of cylindrical, elliptical and spherical particles.

DISCUSSION

The studies conducted on the steel subjected to ECAP demonstrated a significant increase in strength, a decrease in ductility and an increase in corrosion rate, which were caused directly by structural changes. In particular, it was found that ECAP treatment led to a reduction in ferrite grain size down to the nanometer range. Moreover, at higher degrees of ECAP processing, the grains themselves acquired an equiaxed shape. The grain refinement observed by microscopy methods during ECAP treatment is consistent with the reduction of the CSD size obtained by the mW-H and mW-A techniques (Table 5). The investigations also revealed that, along with structural refinement, a dynamic ageing process occurred after ECAP treatment of the steel. This fact is corroborated by evidence that, during the formation of the UFG structure of steel, the precipitation

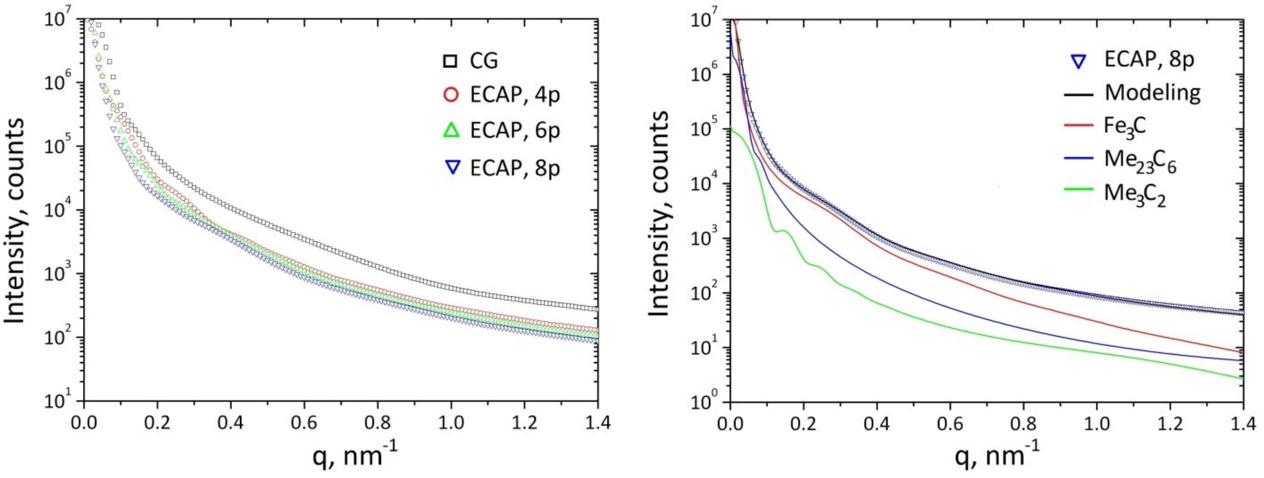

a ***b***

Fig. 6. *Experimental small-angle X-ray scattering curves of steel:*
a *– general view of curves for different structural states;*
b *– processed small-angle X-ray scattering curve of steel (8 ECAP passes)*
Рис. 6. *Экспериментальные кривые малоуглового рентгеновского рассеяния стали:*
a *– общий вид кривых для различных структурных состояний;*
b *– обработанная кривая малоуглового рентгеновского рассеяния стали (8 проходов РКУП)*

Table 6. *Average size and morphology of precipitates obtained by small-angle X-ray scattering method. Particle sizes are given in nanometers*
Таблица 6. *Средний размер и форма преципитатов, полученных методом малоуглового рентгеновского рассеяния. Размерность частиц указана в нанометрах*

State	Fe_3C	$Me_{23}C_6$	Me_3C_2
	Cylinder *d*/*l*	**Ellipse a_1/a_2**	**Sphere *d***
CG	113/384	10/6	–
ECAP, 4 passes	157/431	57/34	31
ECAP, 6 passes	223/458	94/69	49
ECAP, 8 passes	259/460	139/98	72

and growth of $Me_{23}C_6$- and Me_3C_2-type precipitates, as well as a slight increase in the mass fraction of cementite particles were observed (Table 3). As a rule, the dynamic ageing process in steel should lead to the purification of the ferrite crystal lattice from impurity elements, which should be accompanied by a change in the lattice parameter of the base matrix. Indeed, the observed decrease in the ferrite lattice parameter confirms this (Table 5). It is known that the tabular value of the pure ferrite lattice parameter is 0.286 nm [25]. In the initial state, the presence of impurity elements in ferrite led to an increase in the lattice parameter up to 0.286808 nm (Table 5). However, after 8 ECAP passes, the lattice parameter decreased to 0.286692 nm, bringing it closer to the value characteristic of pure ferrite.

Along with the aforementioned changes, the microstructure of the steel after ECAP was characterised by a high density of introduced defects (Table 5). In particular, compared to the initial state, the dislocation density increased significantly after 8 ECAP passes. At the same time, the dislocation type changed as well. Whereas in the initial state the dislocations were mainly of screw type, after 8 ECAP passes they predominantly consisted of edge-type dislocations (Table 5). The obtained data on the degree and type of structural defectiveness is consistent with previous studies [26; 27], according to which, under conditions of severe plastic deformation, an intense annihilation process of screw dislocations within the grain interiors occurs, while the accumulation of edge dislocations at grain boundaries increases and sometimes they form cell walls. To verify this theory, changes in R_e and M parameters were evaluated (Table 5). It is known [28] that R_e parameter characterises the degree of screening of the long-range strain fields of dislocations by adjacent dislocations. In this regard, the decrease in R_e value during ECAP indicates an increase in the degree of screening of dislocation long-range fields, which can result in the formation of dipoles. This phenomenon leads to correlated dislocation interactions, which, as is known, cause the formation of a cellular structure [29].

At the same time, the dimensionless Wilkens parameter $M = R_e\sqrt{\rho}$ characterises the mutual arrangement of dislocations within the grains and determines the strength of the dislocation dipole field [28]. In the initial CG state, the M parameter was close to 2, indicating a chaotic arrangement of dislocations and a weak dipole field. Conversely, after ECAP, this parameter dropped sharply (M<1), indicating an ordered arrangement of dislocations in the steel structure. In general, the decrease in the Wilkens parameter after ECAP treatment indicates the formation of dislocation tangles and dislocation walls in the steel structure leading to the formation of a cellular structure [18]. Some areas of cellular structures within the ferrite grains were also revealed by TEM investigations (Fig. 1).

Thus, according to the obtained data, ECAP treatment leads to an increase in dislocation density, dipole field strength and the degree of dislocation ordering, which ultimately results in the formation of a cellular structure. Subsequently, the cellular structure transforms into grain boundaries [1]. In this context, ferrite grain refinement during ECAP proceeds according to the mechanism schematically shown in Fig. 7.

The conducted structural studies also make it possible to analyse and identify the causes of the increase in the corrosion rate of the steel subjected to ECAP. It is well known [1; 3] that UFG metallic materials are characterised by an increased volumetric fraction of grain boundaries due to grain refinement. The analysis showed that the grain boundaries in the UFG steel contain a high density of dislocations, predominantly of edge type. It is known that the diffusion coefficient along dislocation cores is several orders of magnitude higher compared to the lattice diffusion coefficient [30]. This circumstance leads to the fact that grain boundaries in the UFG steel should exhibit an enhanced diffusion coefficient. As a result, impurity atoms (H, O, S, etc.), which chemically react with Fe, may diffuse along grain boundaries in the UFG steel much faster than in its CG analogue. Accordingly, it can be expected that the formation of the UFG structure with a high density of grain-boundary dislocations is the reason for the increased corrosion rate of the steel subjected to ECAP.

The obtained data on the microstructural parameters of the steel also enable the assessment of the contribution of individual strengthening mechanisms after ECAP processing. It is known that the tensile strength of steels is determined by the action of various strengthening mechanisms, including strengthening due to the initial yield stress σ_o, grain-boundary strengthening σ_{gb}, precipitation strengthening σ_{pp}, solid solution strengthening σ_{ss} and dislocation strengthening σ_d [31]. Based on the obtained microscopy and XRD analysis data, a theoretical evaluation of individual strengthening mechanisms was performed and the resulting tensile strength was calculated. The comparative contribution of individual strengthening components to the resulting tensile strength is presented in Table 7.

When calculating the steel precipitation strengthening σ_{pp} in the CG state, two types of particles were considered, while three types were considered after ECAP processing and the total strengthening $\Sigma\sigma_{pp}$ was determined (Table 3, 6). As previously shown in [31], a theoretical evaluation of the resulting tensile strength requires the use of the root-mean-square $\sqrt{\sum \sigma_i^2}$ summation of the strengthening components. Accordingly, in the present study, the resulting tensile strength was calculated using this summation method. The calculated resulting tensile strength values for the studied states are given in Table 7. As can be seen from Table 7, the resulting tensile strength $\sqrt{\sum \sigma_i^2}$ values for the CG and ECAP-processed states of the steel are in good agreement with the experimental data (Table 2). The analysis of the strengthening mechanisms showed that in the UFG state, the increase in the tensile strength of the steel is primarily due to grain-boundary strengthening σ_{gb} (Table 7). The increase in the contribution of grain-boundary

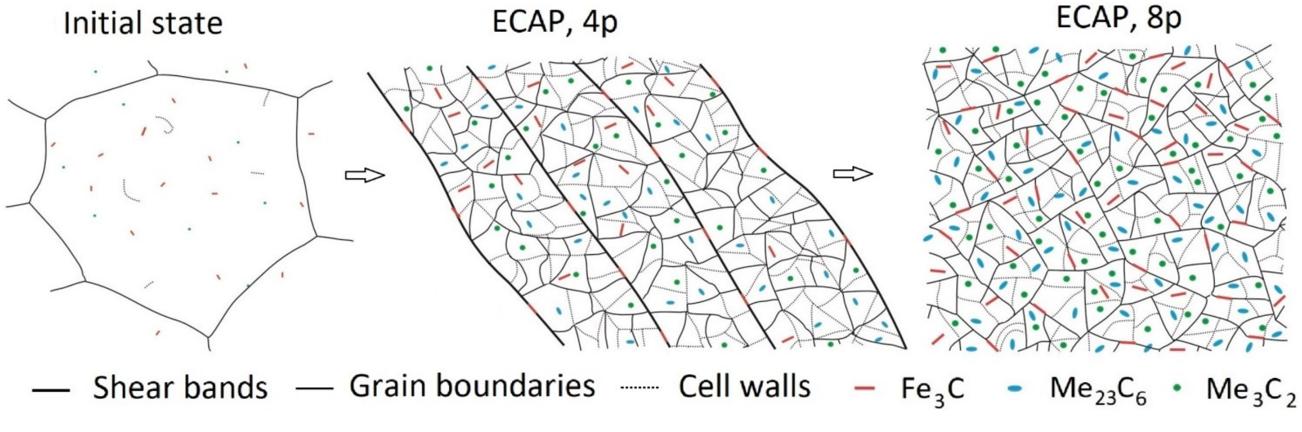

Fig. 7. *Schematic representation of structure transformation during the formation of an ultrafine-grained state in low-carbon steel*
Рис. 7. *Схематичное изображение трансформации структуры при формировании ультрамелкозернистого состояния в низкоуглеродистой стали*

Table 7. *Contribution of different strengthening mechanisms in coarse-grained and ultrafine-grained states of low-carbon steel*
Таблица 7. *Вклад различных механизмов упрочнения в крупнокристаллическом и ультрамелкозернистом состояниях низкоуглеродистой стали*

State	Calculated data, MPa					
	σ_o	σ_{gb}	$\Sigma\sigma_{pp}$	σ_{ss}	σ_d	$\sqrt{\sum \sigma_i^2}$
CG	50	300	268	75	88	419
ECAP, 4 passes	50	916	222	75	366	1015
ECAP, 6 passes	50	946	179	75	431	1059
ECAP, 8 passes	50	951	147	75	480	1079

Note. σ_o *is yield stress;* σ_{gb} *is grain-boundary strengthening;* σ_{pp} *is precipitation strengthening;* σ_{ss} *is solid solution strengthening;* σ_d *is dislocation hardening.*

Примечание. σ_o *– напряжение течения;* σ_{gb} *– зернограничная прочность;* σ_{pp} *– дисперсионная прочность;* σ_{ss} *– прочность твердого раствора;* σ_d *– дислокационная прочность.*

strengthening σ_{gb} after ECAP processing is realised, according to microscopy data, as a result of grain refinement down to the nanometric scale. Moreover, the dislocation strengthening mechanism σ_d also contributes to the enhancement of the tensile strength due to the increased dislocation density after ECAP (Table 5, 7). On the other hand, the contribution of precipitation strengthening $\Sigma\sigma_{pp}$ decreases during the formation of the UFG structure. The analysis showed that in the case of CG steel, the high value of $\Sigma\sigma_{pp}$ is achieved due to the presence of small-sized ellipsoidal $Me_{23}C_6$ particles (Table 6, 7). Meanwhile, the decrease in $\Sigma\sigma_{pp}$ during ECAP is explained by the growth of cementite, $Me_{23}C_6$ and Me_3C_2 particles.

CONCLUSIONS

A high-strength state (ultimate tensile strength of 1072 MPa) with satisfactory ductility (10.7 %) and a corrosion rate of 0.345 mm/year was achieved in the steel using the ECAP method. TEM and XRD analysis identified that the formation of the UFG state is accompanied by grain refinement down to 240 nm, an increase in the dislocation density (predominantly of edge type), precipitation and growth of $Me_{23}C_6$ and Me_3C_2 precipitates and the formation of a dislocation cell structure (reduction of the *M* parameter). In the CG state, steel strengthening is primarily provided by grain-boundary strengthening and the precipitation of relatively small-sized particles (cementite, $Me_{23}C_6$). The increase in the strength of UFG steel is mainly achieved as a result of grain refinement to the nanometric size and an increase in the dislocation density up to $3\cdot10^{15}$ м$^{-2}$. Precipitation strengthening in the UFG state decreases due to the growth in the mass fraction and size of $Me_{23}C_6$ and Me_3C_2 particles. The increase in the corrosion rate of the UFG steel is explained by the small size of ferrite grains containing a high density of grain-boundary dislocations and the presence of a dislocation cell structure.

REFERENCES

1. Zayed E.M., Shazly M., El-Sabbagh A., El-Mahallawy N.A. Deformation behavior and properties of severe plastic deformation techniques for bulk materials: A review. *Heliyon*, 2023, vol. 9, no. 6, article number e16700. DOI: 10.1016/j.heliyon.2023.e16700.
2. Enikeev N.A., Abramova M.M., Smirnov I.V., Mavlyutov A.M., Kim J.G., Lee C.S., Kim H.S. Performance of twinning-induced plasticity steel processed by multipass equal channel angular pressing at high temperatures. *Physical mesomechanics*, 2024, vol. 27, no. 6, pp. 698–709. DOI: 10.1134/S1029959924060079.
3. Figueiredo R.B., Langdon T.G. Deformation mechanisms in ultrafine-grained metals with an emphasis on the Hall–Petch relationship and strain rate sensitivity. *Journal of Materials Research and Technology*, 2021, vol. 14, pp. 137–159. DOI: 10.1016/j.jmrt.2021.06.016.
4. Kasaeian-Naeini M., Sedighi M., Hashemi R. Severe plastic deformation (SPD) of biodegradable magnesium alloys and composites: A review of developments and prospects. *Journal of Magnesium and Alloys*, 2022, vol. 10, no. 4, pp. 938–955. DOI: 10.1016/j.jma.2021.11.006.
5. Li Changsheng, Shao Zhibao, Li Kun, Peng Lianggui, Dong Jingbo. Mechanical properties and plastic deformation mechanisms of Fe–Cr–Ni–Mn–Mo–0.37/0.47 N low magnetic stainless-steel plates. *Materials Chemistry and Physics*, 2025, vol. 344, article number 131114. DOI: 10.1016/j.matchemphys.2025.131114.
6. Levitas V.I. Steady states in severe plastic deformations and microstructure at normal and high pressure. *Journal of Materials Research and Technology*, 2025, vol. 36, pp. 382–397. DOI: 10.1016/j.jmrt.2025.03.060.
7. Ranaware P.G. Effect of severe plastic deformation on aging kinetics of precipitation hardening 17–4 stainless steel. *Materials Today: Proceedings*, 2022, vol. 62, part 14, pp. 7600–7604. DOI: 10.1016/j.matpr.2022.04.783.
8. Usmanov E.I., Rezyapova L.R., Valiev R.Z. High-strength state and strengthening mechanisms of ultrafine-grained

titanium. *Physical Mesomechanics*, 2023, vol. 26, no. 5, pp. 483–494. DOI: 10.1134/s1029959923050016.

9. Cho Yeonggeun, Cho Hyung-Jun, Noh Han-Seop, Kim Sung-Ho, Kim Sung-Joon. Strengthening mechanism and martensite transformation behavior in grain-refined low-Ni austenitic stainless steel. *Materials Science and Engineering: A*, 2024, vol. 916, article number 147368. DOI: 10.1016/j.msea.2024.147368.
10. Mohd Yusuf Sh., Chen Ying, Yang Shoufeng, Gao Nong. Microstructural evolution and strengthening of selective laser melted 316L stainless steel processed by high-pressure torsion. *Materials Characterization*, 2019, vol. 159, article number 110012. DOI: 10.1016/j.matchar.2019.110012.
11. Zrník J., Kraus L., Dobatkin S.V. Influence of Thermal Condition of ECAP on Microstructure Evolution in Low Carbon Steel. *Materials Science Forum*, 2007, vol. 558-559, part 1, pp. 611–616. DOI: 10.4028/0-87849-443-x.611.
12. Zrnik J., Lapovok R., Raab G.I. Prior thermo-mechanical processing to modify structure and properties of severely deformed low carbon steel. *IOP Conference Series: Materials Science and Engineering*, 2014, vol. 63, article number 012066. DOI: 10.1088/1757-899X/63/1/012066.
13. Wang Jing Tao, Xu Cheng, Du Zhong Ze, Qu Guo Zhong, Langdon T.G. Microstructure and properties of a low-carbon steel processed by equal-channel angular pressing. *Materials Science and Engineering: A*, 2005, vol. 410–411, pp. 312–315 DOI: 10.1016/j.msea.2005.08.111.
14. Hajizadeh K., Kurzydlowski K.J. On the possibility of fabricating fully austenitic sub-micron grained AISI 304 stainless steel via equal channel angular pressing. *Material Today Communications*, 2023, vol. 35, article number 105641. DOI: 10.1016/j.mtcomm.2023.105641.
15. Wauthier-Monnin A., Chauveau T., Castelnau O., Réglé H., Bacroix B. The evolution with strain of the stored energy in different texture components of cold-rolled IF steel revealed by high resolution X-ray diffraction. *Materials Characterization*, 2015, vol. 104, pp. 31–41. DOI: 10.1016/j.matchar.2015.04.005.
16. Hao Ting, Tang Haiyin, Luo Guangnan, Wang Xianping, Liu Changsong, Fang Qianfeng. Enhancement effect of inter-pass annealing during equal channel angular pressing on grain refinement and ductility of 9Cr1Mo steel. *Materials Science and Engineering: A*, 2016, vol. 667, pp. 454–458. DOI: 10.1016/j.msea.2016.04.098.
17. Das Bakshi S., Sinha D., Ghosh Chowdhury S. Anisotropic broadening of XRD peaks of α′-Fe: Williamson–Hall and Warren–Averbach analysis using full width at half maximum (FWHM) and integral breadth (IB). *Materials Characterization*, 2018, vol. 142, pp. 144–153. DOI: 10.1016/j.matchar.2018.05.018.
18. Das S.R., Shyamal S., Shee S.K., Kömi J.I., Sahu P. X-ray line profile analysis of the deformation microstructure in a medium-grained Fe-Mn-Al-C austenitic steel. *Materials Characterization*, 2021, vol. 172, article number 110833. DOI: 10.1016/j.matchar.2020.110833.
19. Schafler E., Zehetbauer M.J., Ungár T. Measurement of screw and edge dislocation density by means of X-ray Bragg profile analysis. *Materials Science and Engineering: A*, 2001, vol. 319-321, pp. 220–223. DOI: 10.1016/S0921-5093(01)00979-0.
20. Sitdikov V.D., Murashkin M.Yu., Valiev R.Z. Full-scale use of X-ray scattering techniques to characterize aged Al-2wt.%Cu alloy. *Journal of Alloys and Compounds*, 2018, vol. 735, pp. 1792–1798. DOI: 10.1016/j.jallcom.2017.11.282.
21. Gubicza J., Ungár T. Characterization of defect structures in nanocrystalline materials by X-ray line profile analysis. *Zeitschrift für Kristallographie – Crystalline Materials*, 2007, vol. 222, no. 11, pp. 567–579. DOI: 10.1524/zkri.2007.222.11.567.
22. Ungár T., Dragomir I., Révész Á., Borbély A. The contrast factors of dislocations in cubic crystals: the dislocation model of strain anisotropy in practice. *Journal of Applied Crystallography*, 1999, vol. 32, pp. 992–1002. DOI: 10.1107/s0021889899009334.
23. Park Soon-Dong, Kim Sung Youb, Kim Daeyong. Ab initio investigations of the interfacial bond of Fe(001)/Al(001). *Materials Today Communications*, 2021, vol. 26, article number 102107. DOI: 10.1016/j.mtcomm.2021.102107.
24. Ren Yang, Zuo Xiaoding. Synchrotron X-Ray and Neutron Diffraction, Total Scattering, and Small-Angle Scattering Techniques for Rechargeable Battery Research. *Small Methods*, 2018, vol. 2, no. 8, article number 1800064. DOI: 10.1002/smtd.201800064.
25. Huyan F., Larker R., Rubin P., Hedström P. Effect of Solute Silicon on the Lattice Parameter of Ferrite in Ductile Irons. *ISIJ International*, 2014, vol. 54, no. 1, pp. 248–250. DOI: 10.2355/isijinternational.54.248.
26. Mughrabi H. Dislocation wall and cell structures and long-range internal stresses in deformed metal crystals. *Acta Metallurgica*, 1983, vol. 31, no. 9, pp. 1367–1379. DOI: 10.1016/0001-6160(83)90007-x.
27. Zehetbauer M. Cold work hardening in stages IV and V of F.C.C. metals – II. Model fits and physical results. *Acta Metallurgica et Materialia*, 1993, vol. 41, no. 2, pp. 589–599. DOI: 10.1016/0956-7151(93)90089-b.
28. Ungár T., Révész Á., Borbély A. Dislocations and Grain Size in Electrodeposited Nanocrystalline Ni Determined by the Modified Williamson–Hall and Warren–Averbach Procedures. *Journal of Applied Crystallography*, 1998, vol. 31, pp. 554–558. DOI: 10.1107/S0021889897019559.
29. Wu R., Zaiser M. Cell structure formation in a two-dimensional density-based dislocation dynamics model. *Journal of Materials Science: Materials Theory*, 2021, vol. 5, article number 3. DOI: 10.1186/s41313-020-00025-x.
30. Sauvage X., Enikeev N.A., Valiev R.Z., Nasedkina Y., Murashkin M.Yu. Atomic-scale analysis of the segregation and precipitation mechanisms in a severely deformed Al–Mg alloy. *Acta Materialia*, 2014, vol. 72, pp. 125–136. DOI: 10.1016/j.actamat.2014.03.033.
31. Islamgaliev R.K., Nikitina M.A., Ganeev A.V., Sitdikov V.D. Strengthening mechanisms in ultrafine-grained ferritic/martensitic steel produced by equal channel angular pressing. *Materials Science and Engineering: A*, 2019, vol. 744, pp. 163–170. DOI: 10.1016/j.msea.2018.11.141.

СПИСОК ЛИТЕРАТУРЫ

1. Zayed E.M., Shazly M., El-Sabbagh A., El-Mahallawy N.A. Deformation behavior and properties of severe plastic deformation techniques for bulk materials: A review // Heliyon. 2023. Vol. 9. № 6. Article number e16700. DOI: 10.1016/j.heliyon.2023.e16700.
2. Еникеев Н.А., Абрамова М.М., Смирнов И.В., Мавлютов А.М., Ким Ю.Г., Ли Х.С., Ким Х.С. Поведение стали с пластичностью, наведенной двойнико-

ванием, при многопроходном равноканальном угловом прессовании при повышенных температурах // Физическая мезомеханика. 2024. Т. 27. № 4. С. 85–99. DOI: 10.55652/1683-805X_2024_27_4_85-99.

3. Figueiredo R.B., Langdon T.G. Deformation mechanisms in ultrafine-grained metals with an emphasis on the Hall–Petch relationship and strain rate sensitivity // Journal of Materials Research and Technology. 2021. Vol. 14. P. 137–159. DOI: 10.1016/j.jmrt.2021.06.016.
4. Kasaeian-Naeini M., Sedighi M., Hashemi R. Severe plastic deformation (SPD) of biodegradable magnesium alloys and composites: A review of developments and prospects // Journal of Magnesium and Alloys. 2022. Vol. 10. № 4. P. 938–955. DOI: 10.1016/j.jma.2021.11.006.
5. Li Changsheng, Shao Zhibao, Li Kun, Peng Lianggui, Dong Jingbo. Mechanical properties and plastic deformation mechanisms of Fe–Cr–Ni–Mn–Mo–0.37/0.47 N low magnetic stainless-steel plates // Materials Chemistry and Physics. 2025. Vol. 344. Article number 131114. DOI: 10.1016/j.matchemphys.2025.131114.
6. Levitas V.I. Steady states in severe plastic deformations and microstructure at normal and high pressure // Journal of Materials Research and Technology. 2025. Vol. 36. P. 382–397. DOI: 10.1016/j.jmrt.2025.03.060.
7. Ranaware P.G. Effect of severe plastic deformation on aging kinetics of precipitation hardening 17–4 stainless steel // Materials Today: Proceedings. 2022. Vol. 62. Part 14. P. 7600–7604. DOI: 10.1016/j.matpr.2022.04.783.
8. Усманов Э.И., Резяпова Л.Р., Валиев Р.З. Высокопрочное состояние и механизмы упрочнения титана с ультрамелкозернистой структурой // Физическая мезомеханика. 2023. Т. 26. № 3. С. 5–17. DOI: 10.55652/1683-805X_2023_26_3_5.
9. Cho Yeonggeun, Cho Hyung-Jun, Noh Han-Seop, Kim Sung-Ho, Kim Sung-Joon. Strengthening mechanism and martensite transformation behavior in grain-refined low-Ni austenitic stainless steel // Materials Science and Engineering: A. 2024. Vol. 916. Article number 147368. DOI: 10.1016/j.msea.2024.147368.
10. Mohd Yusuf Sh., Chen Ying, Yang Shoufeng, Gao Nong. Microstructural evolution and strengthening of selective laser melted 316L stainless steel processed by high-pressure torsion // Materials Characterization. 2019. Vol. 159. Article number 110012. DOI: 10.1016/j.matchar.2019.110012.
11. Zrník J., Kraus L., Dobatkin S.V. Influence of Thermal Condition of ECAP on Microstructure Evolution in Low Carbon Steel // Materials Science Forum. 2007. Vol. 558-559. Part 1. P. 611–616. DOI: 10.4028/0-87849-443-x.611.
12. Zrnik J., Lapovok R., Raab G.I. Prior thermo-mechanical processing to modify structure and properties of severely deformed low carbon steel // IOP Conference Series: Materials Science and Engineering. 2014. Vol. 63. Article number 012066. DOI: 10.1088/1757-899X/63/1/012066.
13. Wang Jing Tao, Xu Cheng, Du Zhong Ze, Qu Guo Zhong, Langdon T.G. Microstructure and properties of a low-carbon steel processed by equal-channel angular pressing // Materials Science and Engineering: A. 2005. Vol. 410–411. P. 312–315 DOI: 10.1016/j.msea.2005.08.111.
14. Hajizadeh K., Kurzydlowski K.J. On the possibility of fabricating fully austenitic sub-micron grained AISI 304 stainless steel via equal channel angular pressing // Material Today Communications. 2023. Vol. 35. Article number 105641. DOI: 10.1016/j.mtcomm.2023.105641.
15. Wauthier-Monnin A., Chauveau T., Castelnau O., Réglé H., Bacroix B. The evolution with strain of the stored energy in different texture components of cold-rolled IF steel revealed by high resolution X-ray diffraction // Materials Characterization. 2015. Vol. 104. P. 31–41. DOI: 10.1016/j.matchar.2015.04.005.
16. Hao Ting, Tang Haiyin, Luo Guangnan, Wang Xianping, Liu Changsong, Fang Qianfeng. Enhancement effect of inter-pass annealing during equal channel angular pressing on grain refinement and ductility of 9Cr1Mo steel // Materials Science and Engineering: A. 2016. Vol. 667. P. 454–458. DOI: 10.1016/j.msea.2016.04.098.
17. Das Bakshi S., Sinha D., Ghosh Chowdhury S. Anisotropic broadening of XRD peaks of α′-Fe: Williamson–Hall and Warren–Averbach analysis using full width at half maximum (FWHM) and integral breadth (IB) // Materials Characterization. 2018. Vol. 142. P. 144–153. DOI: 10.1016/j.matchar.2018.05.018.
18. Das S.R., Shyamal S., Shee S.K., Kömi J.I., Sahu P. X-ray line profile analysis of the deformation microstructure in a medium-grained Fe-Mn-Al-C austenitic steel // Materials Characterization. 2021. Vol. 172. Article number 110833. DOI: 10.1016/j.matchar.2020.110833.
19. Schafler E., Zehetbauer M.J., Ungár T. Measurement of screw and edge dislocation density by means of X-ray Bragg profile analysis // Materials Science and Engineering: A. 2001. Vol. 319-321. P. 220–223. DOI: 10.1016/S0921-5093(01)00979-0.
20. Sitdikov V.D., Murashkin M.Yu., Valiev R.Z. Full-scale use of X-ray scattering techniques to characterize aged Al-2wt.%Cu alloy // Journal of Alloys and Compounds. 2018. Vol. 735. P. 1792–1798. DOI: 10.1016/j.jallcom.2017.11.282.
21. Gubicza J., Ungár T. Characterization of defect structures in nanocrystalline materials by X-ray line profile analysis // Zeitschrift für Kristallographie - Crystalline Materials. 2007. Vol. 222. № 11. P. 567–579. DOI: 10.1524/zkri.2007.222.11.567.
22. Ungár T., Dragomir I., Révész Á., Borbély A. The contrast factors of dislocations in cubic crystals: the dislocation model of strain anisotropy in practice // Journal of Applied Crystallography. 1999. Vol. 32. P. 992–1002. DOI: 10.1107/s0021889899009334.
23. Park Soon-Dong, Kim Sung Youb, Kim Daeyong. Ab initio investigations of the interfacial bond of Fe(001)/Al(001) // Materials Today Communications. 2021. Vol. 26. Article number 102107. DOI: 10.1016/j.mtcomm.2021.102107.
24. Ren Yang, Zuo Xiaoding. Synchrotron X-Ray and Neutron Diffraction, Total Scattering, and Small-Angle Scattering Techniques for Rechargeable Battery Research // Small Methods. 2018. Vol. 2. № 8. Article number 1800064. DOI: 10.1002/smtd.201800064.
25. Huyan F., Larker R., Rubin P., Hedström P. Effect of Solute Silicon on the Lattice Parameter of Ferrite in Ductile Irons // ISIJ International. 2014. Vol. 54. № 1. P. 248–250. DOI: 10.2355/isijinternational.54.248.
26. Mughrabi H. Dislocation wall and cell structures and long-range internal stresses in deformed metal crystals // Acta Metallurgica. 1983. Vol. 31. № 9. P. 1367–1379. DOI: 10.1016/0001-6160(83)90007-x.
27. Zehetbauer M. Cold work hardening in stages IV and V of F.C.C. metals – II. Model fits and physical results // Acta Metallurgica et Materialia. 1993. Vol. 41. № 2. P. 589–599. DOI: 10.1016/0956-7151(93)90089-b.

28. Ungár T., Révész Á., Borbély A. Dislocations and Grain Size in Electrodeposited Nanocrystalline Ni Determined by the Modified Williamson–Hall and Warren–Averbach Procedures // Journal of Applied Crystallography. 1998. Vol. 31. P. 554–558. DOI: 10.1107/S0021889897019559.
29. Wu R., Zaiser M. Cell structure formation in a two-dimensional density-based dislocation dynamics model // Journal of Materials Science: Materials Theory. 2021. Vol. 5. Article number 3. DOI: 10.1186/s41313-020-00025-x.
30. Sauvage X., Enikeev N.A., Valiev R.Z., Nasedkina Y., Murashkin M.Yu. Atomic-scale analysis of the segregation and precipitation mechanisms in a severely deformed Al–Mg alloy // Acta Materialia. 2014. Vol. 72. P. 125–136. DOI: 10.1016/j.actamat.2014.03.033.
31. Islamgaliev R.K., Nikitina M.A., Ganeev A.V., Sitdikov V.D. Strengthening mechanisms in ultrafine-grained ferritic/martensitic steel produced by equal channel angular pressing // Materials Science and Engineering: A. 2019. Vol. 744. P. 163–170. DOI: 10.1016/j.msea.2018.11.141.

УДК 691.714, 539.26
doi: 10.18323/2782-4039-2025-3-73-4

Микроструктура, свойства и механизмы упрочнения низкоуглеродистой стали, подвергнутой равноканальному угловому прессованию

Малинин Андрей Владимирович*[1,3], кандидат технических наук,
заместитель генерального директора по исследованиям
Ситдиков Виль Даянович[1,4], доктор физико-математических наук,
старший эксперт
Лебедев Юрий Анатольевич[2], кандидат физико-математических наук,
старший научный сотрудник

[1]*ООО «РН-БашНИПИнефть», Уфа (Россия)*
[2]*Институт физики молекул и кристаллов Уфимского федерального исследовательского центра РАН, Уфа (Россия)*

***E-mail:** MalininAV@bnipi.rosneft.ru

[3]ORCID: https://orcid.org/0000-0003-1185-5648
[4]ORCID: https://orcid.org/0000-0002-9948-1099

Поступила в редакцию 22.07.2025 *Пересмотрена 29.07.2025* *Принята к публикации 20.08.2025*

Аннотация: В работе методом равноканального углового прессования (РКУП) (8 проходов, 200 °C) сформировано ультрамелкозернистое (УМЗ) состояние в низкоуглеродистой стали, демонстрирующее высокие механические свойства (предел текучести 1021 МПа, предел прочности 1072 МПа, пластичность 10,7 %) наряду с удовлетворительной коррозионной стойкостью (0,345 мм/год). Для объяснения причин повышения прочностных и изменения коррозионных свойств проанализирована микроструктура УМЗ стали методами электронной микроскопии и рентгеновского рассеяния. В частности, методами электронной микроскопии установлено измельчение структуры подвергнутой РКУП стали, в результате которого формируются равноосные зерна со средним размером ~240 нм. Модифицированные рентгеновские методики Вильямсона – Холла и Уоррена – Авербаха применены для получения закономерностей изменения размера областей когерентного рассеяния, плотности ρ и доли f_s дислокаций винтового типа, внешнего эффективного радиуса Re сечения дислокаций и ряда других параметров в низкоуглеродистой стали в зависимости от числа проходов (степени деформации) РКУП. Методами рентгенофазового анализа и малоуглового рентгеновского рассеяния найдены закономерности изменения массовой доли, размера и морфологии различных преципитатов от числа проходов РКУП. На основе полученных данных предложена модель трансформации микроструктуры стали при формировании в ней УМЗ состояния. Обсуждаются механизмы упрочнения крупнокристаллической и УМЗ стали. Обнаружено, что в исходном состоянии прочность стали в основном обеспечивается за счет зернограничного упрочнения и выпадения преципитатов $Me_{23}C_6$ и Me_3C_2 малого размера. Показано, что при формировании УМЗ структуры стали прочность возрастает в результате зернограничного упрочнения и роста плотности дислокаций. Вклад в упрочнение преципитатов в УМЗ состоянии понижается, и это обусловлено их ростом при обработке РКУП. Выявлено, что увеличение скорости коррозии УМЗ стали объясняется уменьшением размера ферритных зерен, повышением плотности зернограничных дислокаций и формированием ячеистой структуры.

Ключевые слова: низкоуглеродистая сталь; феррит; равноканальное угловое прессование; ультрамелкозернистая структура; микроструктура; механизмы упрочнения; рентгеноструктурный анализ; скорость коррозии; малоугловое рентгеновское рассеяние.

Благодарности: Авторы выражают благодарность ПАО «НК «Роснефть» и ООО «РН-БашНИПИнефть» за предоставленную возможность проведения исследований. Авторы также благодарят доктора химических наук А.И. Волошина, кандидата физико-математических наук Ю.Б. Линд, кандидата технических наук Н.Р. Яркееву (ООО «РН-БашНИПИнефть») за обсуждение полученных результатов и ценные замечания при подготовке статьи.

Для цитирования: Малинин А.В., Ситдиков В.Д., Лебедев Ю.А. Микроструктура, свойства и механизмы упрочнения низкоуглеродистой стали, подвергнутой равноканальному угловому прессованию // Frontier Materials & Technologies. 2025. № 3. С. 51–65. DOI: 10.18323/2782-4039-2025-3-73-4.